Structural insights into the catalytic mechanism of granzyme B upon substrate and inhibitor binding

Neha Tripathi, Richard Danger, Mélanie Chesneau, Sophie Brouard, Adèle D Laurent

Structural Insights into the Catalytic Mechanism Granzyme B upon Substrate and Inhibitor Binding

Neha Tripathi,[a] *Richard Danger,*[b,c] *Mélanie Chesneau,*[b,c] *Sophie Brouard,*[b,c,d] *and Adèle D. Laurent*[a*]

[a]Laboratoire CEISAM UMR UN-CNRS 6230, Université de Nantes, Nantes F-44000, France

[b]Université de Nantes, CHU Nantes, Inserm, Centre de Recherche en Transplantation et Immunologie, UMR 1064, ITUN, F-44000 Nantes, France

[c]Labex IGO, 44000 Nantes, France

[d]CIC Biotherapy, CHU Nantes, Nantes, 44093, France.

Running Title: Structural Insights on Human Granzyme B

Corresponding Author: *Adèle D. LAURENT - Université de Nantes, CNRS, CEISAM UMR 6230, F-44000 Nantes, France; Email: Adele.Laurent@univ-nantes.fr; Phone Number:+33(0)251 125743.

KEYWORDS: Human Granzyme B; Serine Proteases; Molecular Dynamics; *In silico* Mutation; Catalytic mechanism.

ABSTRACT

Human granzyme B (hGzmB), which is present in various immune cells, has attracted much attention due to its role in various pathophysiological conditions. The hGzmB activity is triggered at a catalytic triad (His59, Asp103, Ser198), cleaving its specific substrates. To date, the drug design strategy against hGzmB mainly targets the catalytic triad, which causes the non-specificity problem of inhibitors due to the highly conserved active site in serine proteases. In the present work, microsecond classical molecular dynamics simulations are devoted to exploring the structural dynamics of the hGzmB catalytic cycle in the presence of Ac-IEPD-AMC, a known substrate (active hGzmB), and Ac-IEPD-CHO, a known inhibitor (inactive hGzmB). By comparing active and inactive forms of hGzmB in the six different stages of the hGzmB catalytic cycle, we revealed, for the very first time, an additional network of interactions involving Arg216, a residue located outside the conventional binding site. Upon activation, the His59···Asp103 hydrogen bond is broken due to the formation of the Asp103···Arg216 salt bridge, expanding the active site to facilitate the substrate-binding. On the contrary, the binding of inhibitor Ac-IEPD-CHO to hGzmB prevents the Arg216-mediated interactions within the catalytic triad, thus preventing hGzmB activity. *In silico* Arg216Ala mutation confirms the role of Arg216 in enzyme activity, as the substrate Ac-IEPD-AMC failed to bind to the mutated hGzmB. Importantly, as Arg216 is not conserved amongst the various granzymes, the current findings can be a major step to guide the design of hGzmB specific therapeutics.

1 Introduction

Immunological responses can be non-specific innate or adaptive immunity, the ultimate goal being to kill the infectious cells. Cytotoxic T-Lymphocytes (CTLs) and natural killer cells (NK cells) [1] induce cellular apoptosis in such cells notably by the perforin/granzyme mediated pathway [2]. This pathway has attracted much attention due to its diverse therapeutic importance [2] in anticancer drug design [3], control of graft rejection [4], and autoimmune disorders [5,6]. The executive components of the perforin/granzyme pathway are granzymes, which belong to the serine protease (SP) family of enzymes [7]. Among the various granzymes, the human granzyme B (hGzmB) is the most potent one [8,9], and has emerged as a potential drug target due to its functional importance not only in the above-mentioned pathologies [3,5,6,10,11], but also in regulatory mechanisms [12,13], giving emergence to a new active research field. Indeed, substrates like pro-caspase-3, pro-caspase-7, pro-caspase-10, topoisomerase I, BH3 interacting-domain death agonist (BID), *etc*. [14,15] are activated by the hGzmB catalytic action triggering the cellular apoptosis in target cells [16]. Several synthetic fluorogenic caspase-8/granzyme B substrates are also used to experimentally measure the hGzmB enzymatic activity, such as N-Acetyl-Ile-Glu-Pro-Asp-aminocoumarine (Ac–IEPD–AMC), Ac–IETD–AMC, and Ac-IETD-p-nitroanilide (Ac-IETD-pNA) [17,18].

The residue numbering scheme followed in this manuscript is not identical to the usual "serine protease numbering scheme" and is shown in Fig. S1. The hGzmB is composed of two β-barrels forming a substrate-binding site at their junction, characterized by the presence of a catalytic triad formed by His59, Asp103, and Ser198 (Fig. S1 and Fig. S2) [19] The hGzmB active site accommodates substrates having a particular amino acid sequence, *i.e.*, Ile–Glu–(Pro/Thr)–Asp–↓–Xaa–Gly-Xaa-Glu [14], (Xaa: any amino acid and ↓: site of cleavage). This motif is usually referred to as P4–P3–P2–P1–↓–P1`–P2`–P3`–P4`. The catalytic mechanism is well known for the SP family of enzymes [7,20], (Fig. S3). Fig. 1 sums up the key stages involved in the hGzmB catalytic cycle and presents the nomenclature used later in this work. In step 1, substrate recognition occurs at the active site in the apo form (**Apo)**, resulting in the formation of a substrate-bound conformation of hGzmB (**SB**). Thereafter (step 2), a tetrahedral intermediate is created after a nucleophilic attack (Fig. S3) [20], followed by the hydrolysis of the P1-P1` substrate peptide bond (step 3). The latter step results in the cleavage of the substrate into two

fragments, *i.e.*, the acyl intermediate, which is covalently linked to the side-chain hydroxyl oxygen of Ser198 (Ser198-O) in hGzmB, and the amine product, further resulting in the formation of an acyl intermediate bound complex (a transient complex). In step 4, the amine product is released from the transient complex, converting it into another acyl intermediate bound complex (**AIB**). A tetrahedral intermediate is formed in the next step (step 5, Fig. S3), which then allows the formation of a carboxyl product at the active site (**CPB**) followed by its release, regenerating **Apo** for the next cycle of catalysis. The release of amine and carboxyl products has been proposed to be stimulated by water molecules entering the active site [7].

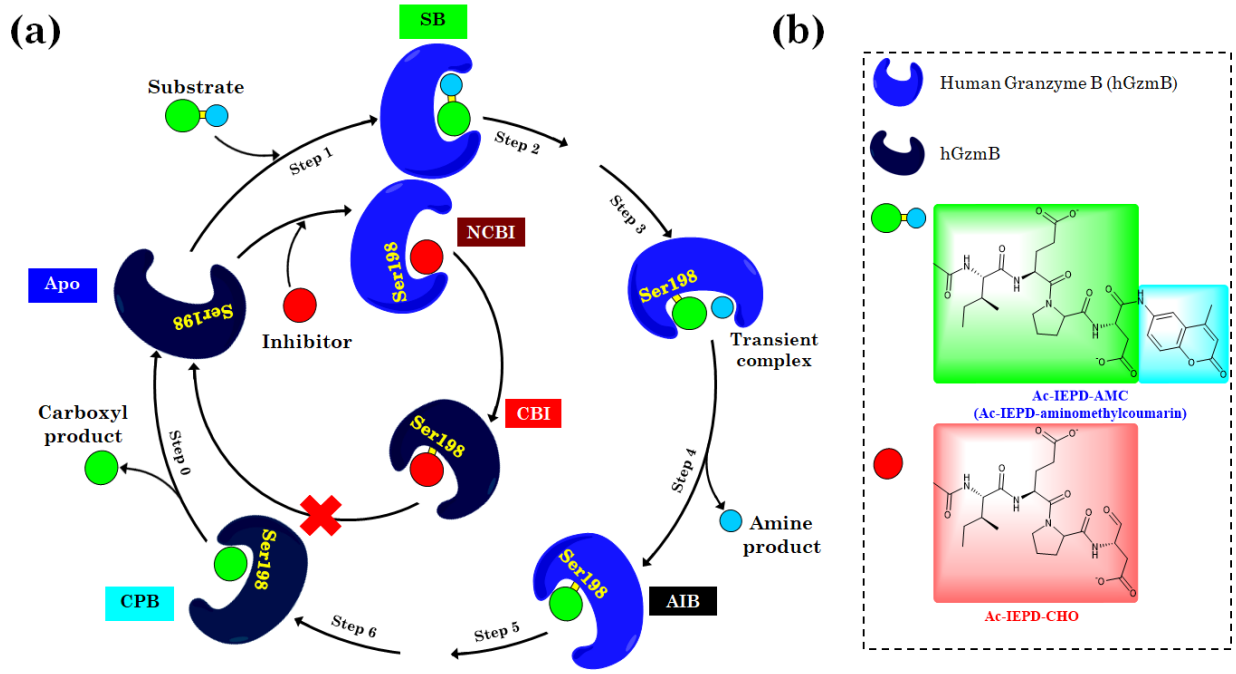

Fig. 1 Catalytic mechanism of hGzmB. (a) Schematic representation for the catalytic cycle of hGzmB. Macromolecular complexes used for molecular modeling are shown in the catalytic cycle. **Apo**: Apoform hGzmB; **SB**: Substrate bound hGzmB; **Transient complex**: Acyl intermediate and amine product bound hGzmB; **AIB**: Acyl intermediate bound hGzmB; **CPB**: Carboxyl product bound hGzmB; **NCBI**: hGzmB-Inhibitor complex (non-covalent); **CBI**: hGzmB-Inhibitor complex (covalent). (b) Legend for Fig.1(a).

In the active field of hGzmB regulations, and particularly in the context of hGzmB inhibition [21,22] (inner cycle of Fig. 1), the hGzmB catalytic action is modulated by molecules/peptides mimicking the hGzmB substrates, which target the catalytic triad and abolish the cleavage function. Such inhibitors are firstly bound non-covalently to hGzmB (**NCBI**), which induces the acylation of hGzmB *via* the Ser198-O, resulting in the formation of a covalently linked hGzmB-

inhibitor complex (**CBI**) blocking the availability of **Apo** for further catalysis. Commonly known hGzmB inhibitors include proteinase inhibitor 9 (also known as SERPINB9) [23], ecotin [24], adenovirus assembly protein L4–100K (100K) [25], Ac–IEPD–CHO (Fig. 1(b)) [21], Ac–IETD–CHO [11], Z–IETD–FMK [26], and 3,4-dichloroisocoumarin [27,28].

On the computational biology side, only a few studies have been reported for such particular interest in hGzmB. Losasso *et al.* [29] employed *in silico* alanine-scanning and short molecular dynamics (MD) simulations to identify key residues involved in the intermolecular interactions between hGzmB and human SERPINB9 (hSB9), and subsequently designed hSB9 resistant recombinant hGzmB variants which should have promising anti-tumoral activity [29]. Peptides mimicking the natural substrates of hGzmB have been explored for the enzyme inhibition, while the inhibition specificity is yet underexplored. Willoughby *et al.* [22] performed structural modulation of Ac-IEPD–CHO inhibitor [21] to design a series of small molecular inhibitors for hGzmB. Kim *et al.* [30] reported a systematic approach involving the application of molecular modeling (probe site mapping, shape-based and property-based virtual screening, molecular docking, and MD simulations) and experimental studies (synthesis and bioassays for hGzmB inhibition) to identify a series of potent non-covalent inhibitors of hGzmB.

Despite the current understanding of the hGzmB reaction mechanism, its structural dynamics involved in the interconversion of active and inactive conformations upon recognition of substrates and inhibitors, respectively, have never been investigated while such information could be highly beneficial to specifically target hGzmB and, it will hence be the main focus of the present work. Therefore, a detailed investigation for identifying the crucial differences between the active and inactive conformations of hGzmB is presented herein using long MD simulations of each complex involved in the catalytic cycle. New structural features, specific to the active and inactive conformations of hGzmB as well as the residues involved in the conversion were identified. *In silico* mutational studies have also been performed to ascertain the functional importance of the involved residues in the enzyme mechanism.

2 Materials and methods

2.1 Macromolecular Structure Preparation

Among the various available crystal structures of GzmB available in the RCSB Protein Data Bank (RCSB/PDB) [31] (Table S1), two belong to human, *i.e.*, the hGzmB apoform (PDB ID: 1FQ3, resolution 3.1 Å) [32] and the Ac–IEPD–CHO bound hGzmB (PDB ID: 1IAU, resolution 2.0 Å) [21]. The later structure was used as the starting point for our work, pertaining to its better resolution. The PDB file retrieved from RCSB/PDB follows a residue numbering scheme exhibited a few peculiar issues. These are (a) the residue number 36 is associated with three residues, *i.e.,* Trp36, Asp36A, and Gln36B; (b) the residue number 184 is associated with Asp184 and Gly184A ; and (c) the residue number 188 is associated with Lys188 and Lys188A. In order to perform the molecular modeling studies in this work, we have renumbered the residues so as to have a peculiar residue number associated exclusively with a single amino acid. The residue numbering scheme followed in this manuscript is shown in Fig. S1. Details about the histidine protonation states used for the molecular studies performed herein are provided in the supporting information (Fig. S4 and Table S2). To generate the **Apo** form, the bound ligand Ac–IEPD–CHO was removed from the crystal structure. This structure was submitted to classical MD simulations.

The active conformation of hGzmB (**SB** in Fig. 1(a)) was created by structural modulation of the bound inhibitor Ac–IEPD–CHO [21] using the Ligand Build utility of the Schrödinger software [33], to create the complex with Ac–IEPD–AMC [17,18]. In this complex, Ac–IEPD–AMC was non-covalently linked to hGzmB. For the transient complex (generated after step 3, Fig. 1(a)), P1-Asp in Ac-IEPD was covalently linked (*via* its backbone carbonyl carbon) to the hGzmB Ser198-O, while the covalent bond between Ac-IEPD and AMC was removed. Additionally, **CPB (**Fig. 1(a)) was generated by removing the covalent link between hGzmB and Ac-IEPD in the **AIB** (generated from the transient complex after MD simulations, discussed later).

To model the inactive conformation of hGzmB, the complex between hGzmB and Ac–IEPD–CHO inhibitor was considered (PDB ID: 1IAU, resolution 2.0 Å) [21]. A non-covalently bound complex of Ac–IEPD–CHO, and hGzmB (**NCBI** in Fig. 1(a)) was generated for a deeper understanding of the molecular recognition of inhibitors by hGzmB. Additionally, **CBI** (Fig. 1(a)) was created by covalently linking Ac–IEPD–CHO (through its P1-Asp backbone carbonyl) to hGzmB (*via* the Ser198-O). To ascertain the importance of the identified crucial residues, *in*

silico mutational studies were further undertaken. For this purpose, Arg216Ala mutation was incorporated, with the help of the Schrödinger software [33], in the **Apo** hGzmB and **SB** complex to generate **Arg216Ala-Apo** and **Arg216Ala-SB**, respectively**.**

2.2 Molecular Dynamics Simulations

Generated complexes were submitted to MD simulations using the NAMD 2.12 software [34]. For all systems, the Charmm36 force field [35] was employed, and explicit solvent molecules were added using the TIP3P water model [36]. All systems were neutralized by the equivalent number of counterions. An additional number of ions Na^+ and Cl^- were included to maintain the physiological ionic concentration [37]. The topology and structural parameters for the covalent bonds between hGzmB and bound ligands were generated using the ParamChem server by employing Charmm General Force Field (CGenFF) (Fig. S5-S6) [38–42].

All the complexes were submitted to a restrained energy minimization (in which only the positions of solvent molecules and ions were relaxed) and to an unrestrained energy minimization (in which the whole system was relaxed), sequentially. Thereafter, equilibration was performed (NVT ensemble, duration: 1 ns), followed by a production run (NPT ensemble, duration: 1μs) for all complexes. All simulations were carried out with a 2 fs time step, at a temperature of 310 K (maintained using Langevin thermostat) [43] and a pressure of 1.013 bar (scaled using the Nosé-Hoover-Langevin piston method) [44]. Periodic boundary conditions were used and long-range electrostatic interactions were treated by the particle mesh Ewald method [45] (cutoff of 12 Å and switch function = 10 Å). All covalent bonds containing hydrogen atoms were constrained using the SHAKE algorithm [46]. The PTRAJ module [47] of Amber tools [48] and Visual Molecular Dynamics software (VMD) [49] were employed for the trajectory analyses. System equilibration parameters, which include the analysis of the root mean square deviation (RMSD) of the system and the atomic fluctuations, helped to ascertain that each system was equilibrated and stabilized after 500 ns of production run (Fig. S7). Therefore, hydrogen bond (H-bond) and salt bridge analyses were carried out after 500 ns of the production run for all investigated systems. The total simulation time, considering all investigated systems is 8 μs.

3 Results and discussion

3.1 Modeling the various stages of the hGzmB catalytic cycle

Various stages of the hGzmB catalysis (Fig. 1) were explored through MD simulations. Six systems were submitted to classical MD simulations, *i.e.*, (i) **Apo** hGzmB, (ii) the substrate-bound **SB**, (iii) the transient complex formed after step 3, (iv) **CPB**, (v) **NCBI**, and (vi) **CBI**. The initial conformation of hGzmB and final conformation of the various complexes at the end of the MD run are shown in Fig. S8 and Fig. S9, respectively. First, we analyzed the main intermolecular interactions between the bound ligands and hGzmB, in various complexes, at the active site in particular *i.e.* inter-molecular interaction analysis, distance between residues, number of H-bonds, and the occurrence frequency of these H-bonds (Fig. S10-S13 and supporting information). As in the reported mechanism for hGzmB, the formation of a covalent linkage between the hGzmB Ser198-O and substrate P1-Asp is a critical step for catalysis. In **SB**, a distance of *c.a.* 4 Å between the hGzmB Ser198-O and the substrate P1-Asp carbonyl carbon was rapidly observed (Fig. S11(a)), which can facilitate the covalent complex formation, as in the known reaction catalysis mechanism for SPs [20]. In our simulation study, the transient complex from the catalytic cycle of hGzmB (Fig. 1) exhibited a release of AMC from the active site (distance between P1-Asp and P1`-AMC increased from *ca.* 4 to 45 Å, Fig. S12) after 400 ns of the production run, as expected from the known mechanism. This converted the transient complex into **AIB**, thus modeling step 4 from the catalytic cycle. In the **CPB** complex, the peptide fragment (*i.e.*, the non-covalently bound carboxyl product) remained at the substrate-binding site of hGzmB till 400 ns, maintaining a small distance (*ca.* 4 Å) between hGzmB Ser198-O and P1-Asp of the product (Fig. S11(a)). Thereafter, **CPB** was destabilized and at 400 ns, the non-covalently bound carboxyl product was released from the active site (increasing the distance between hGzmB Ser198-O and the product P1-Asp from *ca.* 4 to 18 Å, Fig. S11(a)), mimicking step 0 in the catalytic cycle of hGzmB (Fig. 1). The structural superimposition of the last frame after the MD simulations (which belonged to the most populated cluster) for **SB**, **AIB**, and **CPB** (Fig. S11(b)) shows relative positions of the associated ligands. In **CPB**, the P1-Asp residue (ball and stick representation in cyan color, Fig. S11(b)) of the Ac-IEPD is located completely outside the active site of hGzmB, indicating the release of carboxyl product. In **NCBI**, which functionally mimics the **SB**, the distance between the hGzmB Ser198-O and the substrate P1-Asp carbonyl carbon was also stabilized to *ca.* 4 Å (Fig. S11(a)). From this first

rapid analysis of all the investigated systems of the catalytic cycle, the MD simulations of the models reproduced the known global and local features of the hGzmB catalysis.

Further, we superimposed the last frame (which belonged to the most populated cluster) of each complex after MD simulations, to investigate the global deviations in the 3D structures, specifically between the substrate-bound "active" conformation (**SB**) and the inhibitor bound "inactive" conformation (**CBI**). The overall conformation of hGzmB in **CPB**, being the last complex in the catalytic cycle, was similar to the one of **Apo** (RMSD < 1.5 Å, Fig. S14(a)), indicating the regeneration of the **Apo** form for the next cycle of the catalysis. Interestingly, we observed two groups based on RMSD, which exhibited a similar structural pattern, *i.e.*, (i) first one with **Apo**, **CPB,** and **CBI** (Fig. S14(a), RMSD < 2 Å), and (ii) second one with **SB**, the transient complex (converted to **AIB** after MD), and **NCBI** (Fig. S14(b), RMSD between 2 to 3 Å). A major difference was observed at the helix α3 between the groups. Thus, it can be proposed that **Apo**, **CPB**, and **CBI** are within an inactive conformation of hGzmB, whereas **SB**, **AIB**, and **NCBI** are the active ones. Such a hypothesis is guided by the fact that **SB** and **CBI** are known to be in the active and inactive forms, respectively. A global analysis of the various complexes indicated that substrate recognition is associated with several conformational changes in the enzyme. The major one was observed at the helix α3 (see Fig. S8 for nomenclature) in **Apo** and **SB** when compared between the representative states of the active and the inactive forms of hGzmB. A slight bend was evident between Phe231 and Val232 (Fig. S15) in **Apo**, but not in **SB**, which is associated with fluctuations at the active site by a chain of events involving several residues. The structural dynamics of the catalytic triad residues were therefore evaluated in detail in the subsequent sections, to have a closer look at the transduction of observed bend in helix α3.

3.2 **Increased His59:Ser198 distance opening the active site for substrate recognition**

Analysis of the structural parameters for the catalytic triad of hGzmB (formed by His59, Asp103, and Ser198) allowed us to identify the intricate details of the conformational dynamics in hGzmB. The distance between His59-$N_{\varepsilon 2}$ and Ser198-O in the various structures revealed an interesting pattern (Fig. S16). In the complexes **Apo**, **SB**, **AIB**, and **CPB,** the average His59:Ser198 distance (over the last 700 ns) was measured as *ca.* 4, 8, 7, and 4 Å, respectively (Fig. S16(a)). Particularly, the observed His59:Ser198 distances support the fact that **CPB** shows

the same structural pattern (4 Å) as in **Apo**, while **SB** and **AIB** exhibit a similar pattern with a distance of 7 and 8 Å between His59-$N_{\varepsilon 2}$ and Ser198-O, assigning **AIB** as the active conformation.

The increased His59:Ser198 distance in **SB** can be attributed to the reorientation of the hydroxyl group from Ser198 towards the P1-Asp residue of the substrate to facilitate the reaction catalysis. Such results suggest that the inactive **Apo** hGzmB is converted to its active form upon binding of the substrate *via* a conformational change in the side-chains of His59 and Ser198, increasing the distance between these amino acids to accommodate the approaching ligands. The covalent linking between Ac-IEPD and hGzmB (as in **AIB**) is maintained at the active state. To understand the enzyme inhibition by exogenous ligands, we evaluated the structure of complexes **NCBI** and **CBI**. In **NCBI** (with non-covalently linked inhibitors), the His59:Ser198 distance was stabilized at *ca.* 6 Å (rather similar to **SB**) (Fig. S16(a)), indicating the activation of the enzyme to facilitate the formation of the covalent bond between hGzmB and the inhibitor. In **CBI** (with covalently bound inhibitor), which is the inactive conformation, the distance between His59 and Ser198 was found to be *ca.* 4 Å (Fig. S16(a)), which resembles **Apo**. This comparative analysis in terms of distances is in line with the previous one, confirming that **Apo**, **CPB**, and **CBI** correspond to a similar and inactive conformation of hGzmB.

Contrary to **AIB**, the presence of the covalently linked inhibitor in **CBI** does not induce activation. Chemically, the ligands in **AIB** and **CBI** are identical, making the two complexes comparable. Despite this, the functional behavior of the two complexes was opposite to each other. To understand the differential behavior of **AIB** and **CBI**, we analyzed the presence of water molecules in the active site (Fig. S17- S18). Interestingly, we noted that the number of water molecules in the vicinity of His59 and Asp103 was higher in **AIB** (4 and 6, respectively), as compared to in **CBI** (2 and 3, respectively) (Fig. S17(a)-S17(b)). Such an observation was also in correlation with the reported reaction mechanism, wherein water mediates the proton transfer between His59 and the reaction center for **AIB** [50]. For the Ser198 of hGzmB and P1-Asp of ligands, the **CBI** exhibited a larger number of water molecules (6 and 8, respectively), and H-bonds with water as compared to **AIB** (6 and 4, respectively) (Fig. S17(c)-S17(d)). In the same line, the evaluation of H-bonds between the catalytic triad and water molecules in the active site showed that His59 exhibited a single hydrogen bond with water in **AIB**, which was

absent in **CBI** (Fig. S18(a)-S18(c)). In **AIB**, Asp103 was involved in 3 H-bonds with water as compared to 2 in **CBI** (Fig. S18(d)-S18(f)). This trend was reversed for Ser198 in the two complexes, where **CBI** exhibited 2 stable H-bonds, whereas **AIB** exhibited none (Fig. S18(g)-S18(i)). Possibly, the presence of water molecules between His59 and the ester linkage in **AIB** could also be a responsible factor for the observed similar behavior of **SB** and **AIB**.

A closer look at His59 and Ser198 revealed the opening of the active site cavity allowing accommodation of the substrates (increased inter-distance, Fig. S16(b)) and thus facilitates molecular recognition of small molecules. In the presence of the non-covalently linked inhibitor **NCBI**, the His59:Ser198 distance was highly fluctuating along the simulation run with an average distance of *ca.* 6 Å (maroon in Fig. S16(a)), indicating that the non-covalent complexation between hGzmB and the inhibitor does not contribute to inactivation. The formation of **CBI** is responsible for the altered water dynamics at the active site and thus the inactivation of the enzyme. It can be concluded that an increased distance between the $N_{\varepsilon 2}$ of His59 and Ser198-O results in the activation of the enzyme.

3.3 **His59 χ2 angle differentiating the active and inactive forms**

To understand the cause of the increased distance between His59 and Ser198, we have analyzed the torsion angle parameters of His59, which is present in Loop B of hGzmB (Fig. S8). No significant variation in the backbone φ and ψ torsion angles was observed for His59 in the various complexes (Fig. S19(a)-S19(b)). It is also evident from the 3D structure of hGzmB, in which Loop B adopted a highly overlapping conformation in the various structures (Fig. S19(c)). Interestingly, Loop B exhibited a specific geometry due to the presence of two H-bonds between the i^{th} and $i+3^{th}$ residues (Ala57···Cys60 and Ala58···Trp61) (Fig. S20) resulting in a lock, in Loop B, stabilizing the specific 3_{10} helical geometry for all the complexes.

In the available granzyme crystal structures (Table S1), the orientation of the histidine side-chain from the catalytic triad is governed by the occupancy of the active site. The crystallographic structures of GzmB exhibited a similar orientation of His59 imidazole ring in **Apo** hGzmB (PDB ID: 1FQ3) [32] and ecotin bound rat GzmB (PDB ID: 1FI8) [24], which was different from the inhibitor bound form of hGzmB (PDB ID: 1IAU)[21] (Fig. S21). This provides a hint towards the important role of the His59 side-chain orientation in the

conformational dynamics of hGzmB. Let us add that the histidine (equivalent to His59 from hGzmB) reorientation has been reported to be involved in the activation of various SPs [51], and other enzymes [52]. The analysis of the side-chain torsion angles showed that the average χ2 angle (averaged based on cluster population) for His59 was approximately 88, −94, −74, and 99° in the **Apo**, **SB**, **AIB,** and **CPB**, respectively (Fig. 2(a) and Fig. S22). On one hand, in **NCBI**, the χ2 angle of −77° (maroon in Fig. S22) was equivalent to the one in the active conformations **SB** and **AIB** (green and black, respectively, in Fig. 2(a)), indicating the initial event of ligand recognition and enzyme activation for the formation of the covalent acyl adduct with inhibitor. On the other hand, a covalent linking of the inhibitor to the hGzmB *via* the Ser198-O in **CBI** resulted in bringing the His59 χ2 angle of 93° (red in Fig. 2(a)) close to that in **Apo** (blue in Fig. 2(a)).

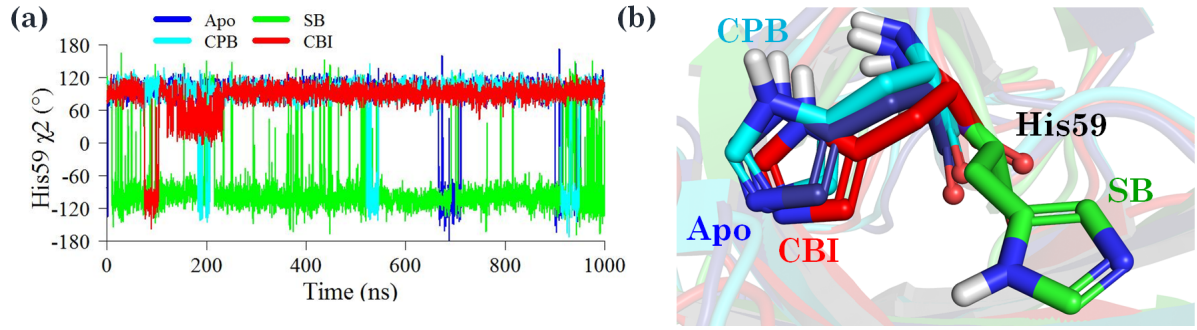

Fig. 2. Analysis of His59 conformation in **Apo** (blue), **SB** (green), **CPB** (cyan), and **CBI** (red). (a) The χ2 during the MD simulations, and (b) Structural superimposition of the last frames after MD simulations to compare His59 orientation.

The structural superimposition of His59 in the various complexes shows that **Apo**, **CPB**, and **CBI** exhibit a similar orientation of His59 side-chain (Fig. 2(b)). The activation of hGzmB, causing the formation of **SB** and **AIB**, induced a flip of the His59 side-chain imidazole ring (Fig. 2(b)). **NCBI** exhibited a His59 side-chain orientation similar to that in **SB**, indicating the activation of the enzyme, which is necessary for the formation of the covalent link between the inhibitor and hGzmB. In **CBI**, the His59 side-chain was reoriented to overlap with **Apo**. It can thus be proposed that the His59 side-chain χ2 angle is crucial to identify the functional state of hGzmB.

3.4 **Loss of His59···Asp103 H-bond as a key phenomenon in enzyme activation**

Further, the residues involved in direct interaction with His59 are investigated to evaluate the consequences and causes of the His59 side-chain flip. The intramolecular H-bonds involving His59 from hGzmB (Fig. 3(a) and Fig. S23(a)) showed that **Apo** was characterized by the presence of a stable H-bond with Asp103 during the entire simulation. Activation of hGzmB resulted in the loss of this interaction (23% occupancy in **SB** and 0% occupancy in **AIB**). The inactive conformation **CBI** was characterized by the presence of a very stable H-bond between His59 and Asp103 (132% occupancy), which is also observed in **Apo**. The distance between His59 ($HN_{\delta 1}$) and Asp103 (C_{δ}) (Fig. S23(b)-S23(c)) was found to be < 4 Å in the complexes representing the inactive conformation (**Apo**, **CPB**, and **CBI**). Such a short distance facilitated the formation of the His59···Asp103 H-bond in **Apo**, **CPB**, and **CBI** (Fig. 3(b), 3(d), and S23(e)). The active conformations **SB**, **AIB**, and **NCBI** exhibit a larger distance of > 6 Å between His59 ($HN_{\delta 1}$) and Asp103 (C_{δ}), indicating the breaking of the H-bond between the two residues upon activation (Fig. 3(c), S23(d), and S23(f)). From such an analysis, it is crystal clear that the breaking of His59···Asp103 H-bond results in the reorientation of the His59 side-chain imidazole ring. An increased distance between the catalytically important residues, *i.e.*, His59, Asp103, and Ser198 indicates an opening of the substrate-binding site for substrate recognition by hGzmB to generate the **SB** complex. In the presence of the covalently linked small molecular inhibitor Ac-IEPD-CHO (**CBI** complex), the His59···Asp103 H-bond was present, whereas, in the presence of covalently linked acyl-intermediate (**AIB** complex), this H-bond was lost. Therefore, the viability of the His59···Asp103 H-bond is induced by the functional state of the enzyme and not by the occupancy of the active site.

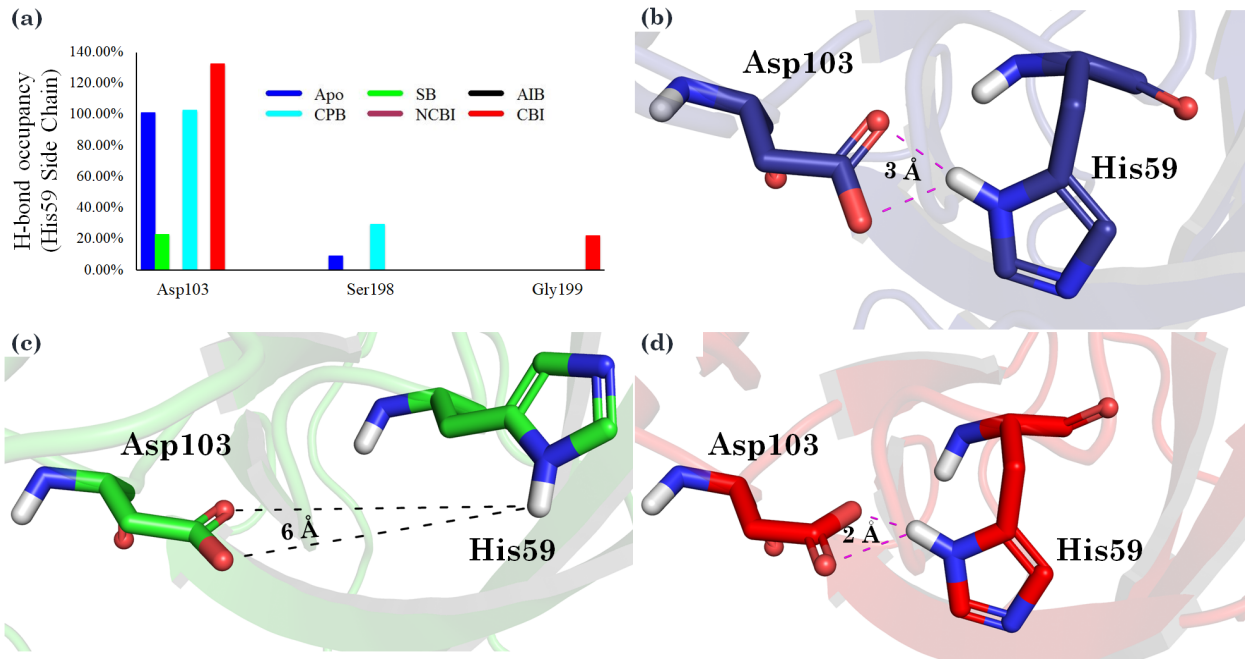

Fig. 3. Interaction between His59 and Asp103 during the MD simulations. (a) Occupancy analysis of the H-bond involving the His59 side-chain in the various complexes. The relative orientation of His59 and Asp103 in (b) **Apo**, (c) **SB**, and (d) **CBI**. Distances are shown in magenta (when H-bond is possible) and black (when H-bond is not possible).

3.5 Formation of Asp103···Arg216 salt bridge inducing a loss of the His59···Asp103 H-bond

To identify the atomic phenomenon which initiates the breaking of the His59···Asp103 H-bond, intramolecular non-bonded interactions of hGzmB were examined in the various complexes. Overall, 33 pairs of salt bridges between acidic and basic residues were found in the complexes (Fig. S24), of which five salt bridges, *i.e.*, Asp51···Arg115, Asp52···Arg50, Asp52···Lys112, Glu157···Arg27, and Glu157···Lys159, were present in all complexes considered in the MD simulations. Among the 28 random salt bridge interactions, present in the various complexes, Asp103···Arg216 and Glu188···Lys190 bridges were present only in the active conformations, *i.e.*, **SB** and **AIB**, whereas the other macromolecular structures lacked these two interactions (Fig. S24). It can be noted that Lys190 and Arg216 were also involved in the formation of three more salt bridge pairs, Asp171···Arg216, Glu181···Arg216, and Asp186···Lys190. Considering the importance of Asp103···Arg216 and Glu188···Lys190, these salt bridges were analyzed in more detail for all the complexes.

The Glu188···Lys190 salt bridge interaction was not stable in **SB** and **AIB**, as the distance between the side-chain centers of the charged residues was highly fluctuating in the two complexes (Fig. S25(a)). To identify the factors responsible for this destabilization, we particularly analyzed the location of Glu188 and Lys190 in **SB**. These residues are situated at the surface of the enzyme (Fig. S26(a)) and are thus accessible to the solvent. Interestingly, the number of water molecules, which surrounded the carboxylate group of Glu188, is directly proportional to the distance between the side-chain of Glu188 and Lys190 (Fig. S26(b)). An intermittent breaking of the Glu188···Lys190 salt bridge was caused by the formation of H-bond interactions between the Glu188 side-chain and surrounding water molecules (Fig. S26(c) and Fig. S26(d)). This salt bridge thus cannot be proposed to take part in the conversion of the inactive to the active conformation.

In the inactive conformations of hGzmB, *i.e.*, **Apo**, **CPB**, and **CBI**, no Asp103···Arg216 salt bridge could be observed (Fig. S24). Contrarily, **SB,** and **AIB** exhibited this particular salt bridge, which was formed after 550 and 400 ns, respectively (Fig. 4(a), indicated by a shortened distance between the two residues). The Asp103···Arg216 distance (measured from the center of mass of the side-chain functional groups) was found to be *ca.* 8 Å in the **SB** complex and *ca.* 5 Å in **AIB** (Fig. 4(a)) during the simulations, whereas in the other complexes, the distance was remarkably much larger (> 10 Å, Fig. S25(b)). The analysis of the Asp103···Arg216 distance in the **SB** (distance reduced from *ca.* 18 to 8 Å) and **AIB** (distance reduced from *ca.* 18 to 5 Å) complexes pointed towards the pulling of Asp103 towards Arg216.

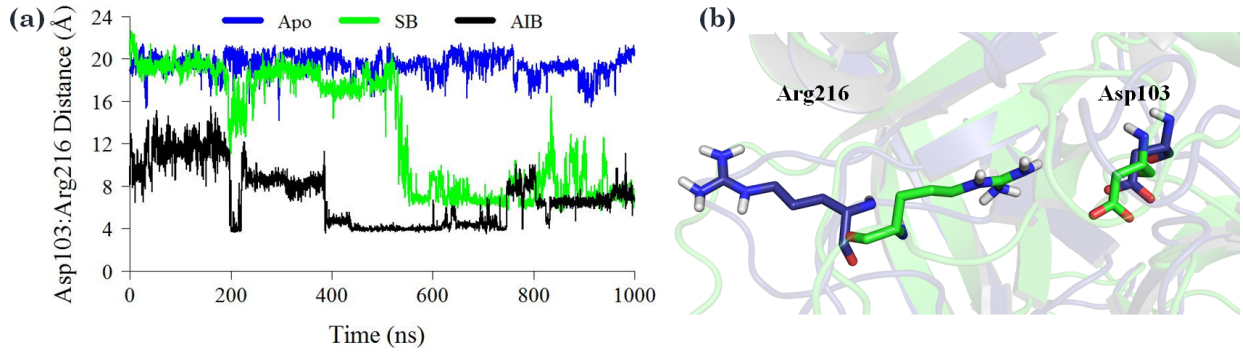

Fig. 4 Detailed investigation of the Asp103···Arg216 salt bridge in **Apo**, **SB**, and **AIB** during the MD simulations. (a) Distance between Asp103 and Arg216 side-chains. (b) Structural superimposition of **Apo** (blue) and **SB** (green) for comparison of the relative orientation of Asp103 and Arg216.

The cavity opening and substrate recognition are thus initiated by the formation of the Asp103···Arg216 salt bridge, which induces breaking of the His59···Asp103 H-bond and subsequently, His59 imidazole ring flipping. As a result, the distance between His59 and Ser198 is increased and significant space is created at the active site to accommodate the substrate. In the inactive conformations, **Apo**, **CPB**, and **CBI**, Arg216 did not exert any conformational change on Asp103 (indicated by the larger distance between the two residues, Fig. 4(a) and Fig. S25(b)) and thus, failed to break the H-bond between His59 and Asp103. The structural superimposition of **Apo** and **SB** complexes (Fig. 4(b)) further supported this hypothesis. This could be responsible for the observed difference in the helix α_3 conformation in active and inactive hGzmB (Fig. S15), where the reorientation of the catalytic triad transmits a conformational change *via.* Ala58, Ile104, and Phe231. With this analysis, Arg216 can thus be proposed as an important amino acid for the inactive to an active conformational change in hGzmB. To confirm the proposed role of Arg216 in substrate recognition, we next undertook the *in silico* mutational studies.

3.6 In silico mutational studies to evaluate the importance of Arg216

To validate the preponderant role of Arg216 in the modulation of the H-bond network at the hGzmB active site, two macromolecular structures were considered, *i.e.*, the apoform Arg216Ala hGzmB (**Arg216Ala-Apo**) and substrate-bound conformation with Arg216Ala mutation (**Arg216Ala-SB**). The analysis of the RMSD for **Arg216Ala-Apo** and **Arg216Ala-SB** showed that during 1μs MD simulations, these systems reached structural stability after 500 ns of production run (Fig. S27(a)-S27(b)). In the wild type **Apo**, Ser198 exhibited at least two stable H-bond interactions, which involved Gly45 (93% occupancy) and His59 (10% occupancy), which are interestingly, also present in **Arg216Ala-Apo** (92% occupancy with Gly45 and 33% occupancy with His59). The distance between the $N_{\varepsilon 2}$ of His59 and Ser198-O was found to be *ca.* 4 Å in **Arg216Ala-Apo** (Fig. S27(c)). The distance between $N_{\delta 2}$ of His59 and C_{δ} of Asp103 was *ca.* 3 Å in **Arg216Ala-Apo** (Fig. 5(a) and S27(d)). The results indicate that the structural integrity of the mutated hGzmB was not altered upon the Arg216Ala mutation. It also supports the proposed hypothesis that in the inactive **Apo** conformation, Arg216 is not able to induce any conformational change at the active site.

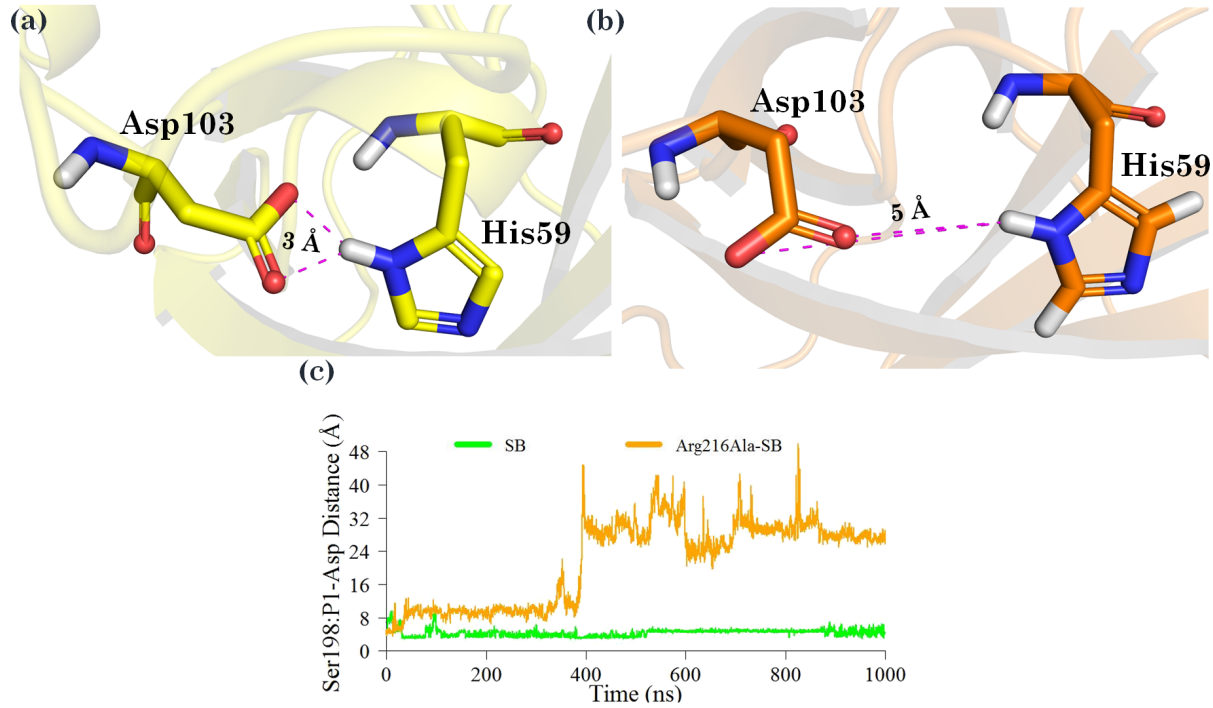

Fig. 5 *In silico* mutational results during the MD simulations. Distance between the $N_{\delta 2}$ of His59 and C_{δ} of Asp103 in (a) **Arg216Ala-Apo** and (b) **Arg216Ala-SB** complex. (c) Distance between Ser198 and P1-Asp residue from the substrate.

In **Arg216Ala-SB**, the distance between $N_{\delta 2}$ of His59 and C_{δ} of Asp103 was highly fluctuating (Fig. S27(d)) and exhibited a decreased length after 500 ns of simulation. Over the last 500 ns, the His59-Asp103 distance was optimized to *ca.* 5 Å (calculated based on cluster population, Fig. 5(b)), which was lower than that in the wild type **SB** complex, *ca.* 6 Å. Therefore, Arg216Ala mutation fails to break the H-bond between His59 and Asp103. In the wild type **SB**, the distance between Ser198-O and P1-Asp residue was optimized to *ca.* 4 Å, while in the **Arg216Ala-SB** mutant, the distance between Ser198 and P1-Asp increased drastically to > 24 Å after 400 ns (Fig. 5(c)). The substrate was already thrown out of the substrate-binding site in **Arg216Ala-SB**. The proposed atomistic phenomenon involving Arg216 as a crucial mediator in the active site opening and substrate recognition is thus supported by the *in silico* mutational studies. The comparative sequence analysis (Table S3) between hGzmB and other granzymes from human (hGzm), mouse (mGzm) and rat (rGzm) showed that the presence of Arg216 is exhibited by hGzmB only (Fig. S28). The rGzmC, mGzmD, mGzmE, hGzmK, and mGzmN

exhibited the presence of a basic residue in this position. This position was highly non-conserved for other granzymes, making the proposed mechanism exclusive for hGzmB.

4 Conclusions

Considering the diversified therapeutic application of the human granzyme B (hGzmB), it becomes crucial to understand, at an atomic level, the enzyme activation by the endogenous substrates and inactivation by the inhibitors. In this context, a total of 8 μs of systematic classical molecular dynamics (MD) simulations were performed to identify the crucial differences between the active and inactive conformations of hGzmB. For this purpose, various stages of the hGzmB catalytic cycle were submitted to MD simulations for 1μs each. The structural comparison was performed between six modeled complexes. An inactive conformation of hGzmB was observed not only for **CBI** but also for **Apo** and **CPB** and was characterized by several structural features. These differentiated it from the active conformation, including the **SB**, **AIB**, and **NCBI**, one of which was the presence of a bend in the helix α3. Fluctuations at the active site are communicated to helix α3 *via* Ala58 and Ile104, removing the bend between Phe231 and Ala232 in the active conformations. In the inactive conformation, the distance between His59 and Ser198 was averaged to *ca.* 4 Å, whereas in the active conformation, this value was larger than 6 Å. The χ2 angle for the Hi59 side-chain was larger than 80° and lower than −70° in the inactive and active conformations, respectively, indicating a flip in the side-chain upon enzyme activation. The inactive conformation was characterized by the presence of an H-bond between His59 and Asp103, *via* their side-chain, whereas this H-bond was missing in the active conformation. Further, the active conformations **SB** and **AIB** exhibited the Asp103···Arg216 salt bridge, which was not observed in any other complex. Based on this thorough analysis, a chain of intramolecular communication upon enzyme activation was illustrated. Substrate recognition by hGzmB induces the formation of a salt bridge interaction between Asp103 and Arg216. It resulted in the breaking of His59···Asp103 H-bond, thus allowing reorientation of the His59 side-chain. An increased distance between the catalytically important residues, *i.e.*, His59, Asp103, and Ser198 following this event, allows the opening of the active site cavity.

The importance of Arg216 was further validated by *in silico* mutational studies, the Arg216Ala mutation failing hGzmB to accommodate the substrate at the active site and to convert it into an active conformation. Results from our work illustrate, for the first time, the importance of Arg216 in initiating enzyme activation. We can propose that the enzyme activation phenomenon is not limited to the active site of the enzyme. The hGzmB presents a peculiar example of such an event, as this residue is a non-conserved one among the various granzyme, wherein the effects of activation are originating from Arg216, which is not a part of the catalytic triad. This can be critical for the identification of novel inhibitors, and our study can be of prime importance to make the anti-hGzmB drug discovery more efficient.

Associated content

Supporting Information. Structural details of the enzyme, computational methodology, stability analysis after MD simulations, Interaction analysis for various ligands, analysis of water molecules in the active site for various complexes, analysis of His59 parameters in detail, salt bridge analysis., mutational studies, and comparative sequence analysis between various granzymes.

Structural coordinates obtained after MD simulations. Apoform hGzmB (Apo.pdb); Substrate bound hGzmB (SB.pdb); Acyl intermediate bound human granzyme B (AIB.pdb); Carboxyl product (Ac-IEPD) bound human granzyme B (CPB.pdb); hGzmB with Non-covalently bound inhibitor (NCBI.pdb); hGzmB with covalently bound inhibitor (CBI.pdb) Apoform hGzmB with Arg216 mutated to Ala216 (Arg216Ala-Apo.pdb); Substrate bound hGzmB with Arg216 mutated to Ala216 (Arg216Ala-SB.pdb)

Conflict of interest

The authors declare no competing financial interest.

Acknowledgment

NT thanks the Région Pays de la Loire and the Centre National de la Recherche Scientifique (CNRS) for the financial support during her post-doctoral research. ADL acknowledges the Régional des Pays de la Loire for financial support within the framework of Mim-Breg. RD, MC,

and SB thanks the IHU-Cesti project (ANR-10-IBHU-005), the DHU Oncogreffe, the LabEX IGO (ANR-11- LABX-0016-01), the ANR project PRELUD (ANR-18-CE17-0019), the ANR project BIKET (ANR-17-CE17-0008), and the ANR project KTD-innov (ANR-17-RHUS-0010) Authors thank the French government financial support managed by the National Research Agency. The IHU-Cesti project was also supported by Nantes Métropole and Région Pays de la Loire. The laboratory received funding from the European Union's Horizon 2020 Research and Innovation Programme under Grant Agreement No. 754995. The authors thank CCIPL (Centre de Calcul Intensif des Pays de Loire) and Aymeric Blondel for the technical support. We are highly grateful to Daniel Vercauteren for his careful reading and fruitful comments. The authors also thank Rui Sousa, Iyanar Vetrivel, and Mohammad Asad for their productive discussion.

Abbreviations

3D	: Three dimensional
Ac–IEPD	: N-Acetyl-Ile-Glu-Pro-Asp-aminocoumarine
Ac-IETD	: N-Acetyl-Ile-Glu-Thr-Asp
Ac-IETD-pNA	: Ac-IETD-p-nitroanilide
AIB	: Acyl intermediate bound human granzyme B
AMC	: Aminocoumarine
Apo	: Apoform human granzyme B
Arg216Ala-Apo	: Apoform human granzyme B with Arg216 mutated to Ala216
Arg216Ala-SB	: Substrate bound human granzyme B with Arg216 mutated to Ala216
CBI	: human granzyme B with covalently bound inhibitor (Ac-IEPD-CHO)
CPB	: Carboxyl product (Ac-IEPD) bound human granzyme B
H-bonds	: Hydrogen bonds
hGzmB	: Human granzyme B
hSB9	: Human SERPINB9
MD	: Molecular Dynamics
NCBI	: human granzyme B with Non-covalently bound inhibitor (Ac-IEPD-CHO)
PME	: Particle Mesh Ewald
RMSD	: Root mean square deviation
SB	: Substrate (Ac–IEPD-AMC) bound human granzyme B
SERPINB9	: Proteinase inhibitor B
VMD	: Visual Molecular Dynamics

References

[1] A. O'Garra, P. Vieira, Regulatory T cells and mechanisms of immune system control, Nat. Med. 10 (2004) 801–805. https://doi.org/10.1038/nm0804-801.

[2] J.A. Trapani, M.J. Smyth, Functional significance of the perforin/granzyme cell death pathway, Nat. Rev. Immunol. 2 (2002) 735–747. https://doi.org/10.1038/nri911.

[3] J.A. Trapani, V.R. Sutton, Granzyme B: Pro-apoptotic, antiviral and antitumor functions, Curr. Opin. Immunol. 15 (2003) 533–543. https://doi.org/10.1016/S0952-7915(03)00107-9.

[4] J. Durand, V. Huchet, E. Merieau, C. Usal, M. Chesneau, S. Remy, M. Heslan, I. Anegon, M.-C. Cuturi, S. Brouard, E. Chiffoleau, Regulatory B Cells with a Partial Defect in CD40 Signaling and Overexpressing Granzyme B Transfer Allograft Tolerance in Rodents, J. Immunol. 195 (2015) 5035–5044. https://doi.org/10.4049/jimmunol.1500429.

[5] L. Casciola-Rosen, F. Andrade, D. Ulanet, W.B. Wong, A. Rosen, Cleavage by granzyme B is strongly predictive of autoantigen status: Implications for initiation of autoimmunity, J. Exp. Med. 190 (1999) 815–826. https://doi.org/10.1084/jem.190.6.815.

[6] E. Darrah, A. Rosen, Granzyme B cleavage of autoantigens in autoimmunity, Cell Death Differ. 17 (2010) 624–632. https://doi.org/10.1038/cdd.2009.197.

[7] J. Kraut, Serine proteases: Structure and mechanism of catalysis, Annu. Rev. Biochem. 46 (1977) 331–358. https://doi.org/10.1146/annurev.bi.46.070177.001555.

[8] D. Kaiserman, C.H. Bird, J. Sun, A. Matthews, K. Ung, J.C. Whisstock, P.E. Thompson, J.A. Trapani, P.I. Bird, The major human and mouse granzymes are structurally and functionally divergent, J. Cell Biol. 175 (2006) 619–630. https://doi.org/10.1083/jcb.200606073.

[9] W.A. Boivin, D.M. Cooper, P.R. Hiebert, D.J. Granville, Intracellular versus extracellular granzyme B in immunity and disease: Challenging the dogma, Lab. Investig. 89 (2009) 1195–1220. https://doi.org/10.1038/labinvest.2009.91.

[10] S. Legros-Maida, A. Soulie, C. Benvenuti, A. Wargnier, N. Vallee, C. Berthou, J. Guillet, M. Sasportes, N. Sigaux, Granzyme B and perforin can be used as predictive markers of acute rejection in heart transplantation, Eur J Immunol. 24 (1994) 229–233.

[11] M. Hayashida, H. Kawano, T. Nakano, K. Shiraki, A. Suzuki, Cell death induction by CTL: Perforin/granzyme B system dominantly acts for cell death induction in human hepatocellular carcinoma cells (44563), Proc. Soc. Exp. Biol. Med. 225 (2000) 143–150.

[12] M. Chesneau, L. Michel, N. Degauque, S. Brouard, Regulatory B cells and tolerance in transplantation: From animal models to human, Front. Immunol. 4 (2013) 497. https://doi.org/10.3389/fimmu.2013.00497.

[13] M. Chesneau, L. Michel, E. Dugast, A. Chenouard, D. Baron, A. Pallier, J. Durand, F. Braza, P. Guerif, D.A. Laplaud, J.P. Soulillou, M. Giral, N. Degauque, E. Chiffoleau, S. Brouard, Tolerant kidney transplant patients produce B cells with regulatory properties, J. Am. Soc. Nephrol. 26 (2015) 2588–2598. https://doi.org/10.1681/ASN.2014040404.

[14] J. Sun, J.C. Whisstock, P. Harriott, B. Walker, A. Novak, P.E. Thompson, A.I. Smith, P.I. Bird, Importance of the P4′ residue in human granzyme B inhibitors and substrates revealed by scanning mutagenesis of the proteinase inhibitor 9 reactive center loop, J.

Biol. Chem. 276 (2001) 15177–15184. https://doi.org/10.1074/jbc.M006645200.
[15] S.P. Cullen, C. Adrain, A.U. Lüthi, P.J. Duriez, S.J. Martin, Human and murine granzyme B exhibit divergent substrate preferences, J. Cell Biol. 176 (2007) 435–444. https://doi.org/10.1083/jcb.200612025.
[16] I.S. Afonina, S.P. Cullen, S.J. Martin, Cytotoxic and non-cytotoxic roles of the CTL/NK protease granzyme B, Immunol. Rev. 235 (2010) 105–116. https://doi.org/10.1111/j.0105-2896.2010.00908.x.
[17] N.A. Thornberry, T.A. Rano, E.P. Peterson, D.M. Rasper, T. Timkey, M. Garcia-Calvo, V.M. Houtzager, P.A. Nordstrom, S. Roy, J.P. Vaillancourt, K.T. Chapman, D.W. Nicholson, A Combinatorial Approach Defines Specificities of Members of the Caspase Family and Granzyme B, J Biol Chem. 272 (1997) 17907–17911. https://doi.org/10.1074/jbc.272.29.17907.
[18] L. Casciola-Rosen, M. Garcia-Calvo, H.G. Bull, J.W. Becker, T. Hines, N.A. Thornberry, A. Rosen, Mouse and human granzyme B have distinct tetrapeptide specificities and abilities to recruit the Bid pathway, J. Biol. Chem. 282 (2007) 4545–4552. https://doi.org/10.1074/jbc.M606564200.
[19] J.L. Harris, E.P. Peterson, D. Hudigi, N.A. Thornberry, C.S. Craik, Definition and redesign of the extended substrate specificity of granzyme B, J. Biol. Chem. 273 (1998) 27364–27373. https://doi.org/10.1074/jbc.273.42.27364.
[20] C.M. Antão, F.X. Malcata, Plant serine proteases: Biochemical, physiological and molecular features, Plant Physiol. Biochem. 43 (2005) 637–650. https://doi.org/10.1016/j.plaphy.2005.05.001.
[21] J. Rotonda, M. Garcia-Calvo, H.G. Bull, W.M. Geissler, B.M. McKeever, C.A. Willoughby, N.A. Thornberry, J.W. Becker, The three-dimensional structure of human granzyme B compared to caspase-3, key mediators of cell death with cleavage specificity for aspartic acid in P1, Chem. Biol. 8 (2001) 357–368. https://doi.org/10.1016/S1074-5521(01)00018-7.
[22] C.A. Willoughby, H.G. Bull, M. Garcia-Calvo, J. Jiang, K.T. Chapman, N.A. Thornberry, Discovery of potent, selective human granzyme B inhibitors that inhibit CTL mediated apoptosis, Bioorganic Med. Chem. Lett. 12 (2002) 2197–2200.
[23] C.H. Bird, V.R. Sutton, J. Sun, C.E. Hirst, A. Novak, S. Kumar, J.A. Trapani, P.I. Bird, Selective regulation of apoptosis: The cytotoxic lymphocyte serpin proteinase inhibitor 9 protects against granzyme B-mediated apoptosis without perturbing the Fas cell death pathway., Mol. Cell. Biol. 18 (1998) 6387–6398. https://doi.org/10.1128/MCB.18.11.6387.
[24] S.M. Waugh, J.L. Harris, R. Fletterick, C.S. Craik, The structure of the pro-apoptotic protease granzyme B reveals the molecular determinants of its specificity, Nat. Struct. Biol. 7 (2000) 762–765. https://doi.org/10.1038/78992.
[25] F. Andrade, H.G. Bull, N.A. Thornberry, G.W. Ketner, L.A. Casciola-Rosen, A. Rosen, Adenovirus L4-100K assembly protein is a granzyme B substrate that potently inhibits granzyme B-mediated cell death, Immunity. 14 (2001) 751–761. https://doi.org/10.1016/S1074-7613(01)00149-2.
[26] H. Toda, T. Yabu, H. Shiba, T. Moritomo, T. Nakanishi, Evaluating antigen-specific cytotoxicity of CD8+ T cells in fish by granzyme B-like activity, Vet. Immunol. Immunopathol. 141 (2011) 168–172. https://doi.org/10.1016/j.vetimm.2011.02.020.

[27] S. Odake, C.M. Kam, L. Narasimhan, J.C. Powers, M. Poe, J.T. Blake, O. Krahenbuhl, J. Tschopp, Human and murine cytotoxic T lymphocyte serine proteases: Subsite mapping with peptide thioester substrates and inhibition of enzyme activity and cytolysis by isocoumarins, Biochemistry. 30 (1991) 2217–2227. https://doi.org/10.1021/bi00222a027.

[28] A. Anel, S. Gamen, M.A. Alava, A.M. Schmitt-Verhulst, A. Pineiro, J. Naval, Inhibition of CPP32-like proteases prevents granzyme B- and Fas-, but not granzyme A-based cytotoxicity exerted by CTL clones, J. Immunol. 158 (1997) 1999–2006. http://www.ncbi.nlm.nih.gov/entrez/query.fcgi?cmd=Retrieve&db=PubMed&dopt=Citation&list_uids=9036942.

[29] V. Losasso, S. Schiffer, S. Barth, P. Carloni, Design of human granzyme B variants resistant to serpin B9, Proteins Struct. Funct. Bioinforma. 80 (2012) 2514–2522. https://doi.org/10.1002/prot.24133.

[30] M.S. Kim, L.A. Buisson, D.A. Heathcote, H. Hu, D.C. Braddock, A.G.M. Barrett, P.G. Ashton-Rickardt, J.P. Snyder, Approaches to design non-covalent inhibitors for human granzyme B (hGrB), Org. Biomol. Chem. 12 (2014) 8952–8965. https://doi.org/10.1039/c4ob01874e.

[31] A. Kouranov, L. Xie, J. Cruz de la, L. Chen, J. Westbrook, P.E. Bourne, H.M. Berman, The RCSB PDB information portal for structural genomics, Nucleic Acids Res. 34 (2006) D302–D305. https://doi.org/10.1093/nar/gkj120.

[32] E. Estébanez-Perpiñá, P. Fuentes-Prior, D. Belorgey, M. Braun, R. Kiefersauer, K. Maskos, R. Huber, H. Rubin, W. Bode, Crystal structure of the caspase activator human granzyme B, a proteinase highly specific for an Asp-P1 residue, Biol. Chem. 381 (2000) 1203–1214. https://doi.org/10.1515/BC.2000.148.

[33] Maestro, Schrödinger, LLC, New York, NY, 2019, (n.d.).

[34] J.C. Phillips, R. Braun, W. Wang, J. Gumbart, E. Tajkhorshid, E. Villa, C. Chipot, R.D. Skeel, L. Kalé, K. Schulten, Scalable molecular dynamics with NAMD, J. Comput. Chem. 26 (2005) 1781–1802. https://doi.org/10.1021/nl061786n.Core-Shell.

[35] X. Zhu, P. Lopes, A. MacKerell, Recent developments and applications of the CHARMM force fields, Wiley Interdiscip. Rev Comput Mol Sci. 2 (2012) 167–185. https://doi.org/10.1002/wcms.74.Recent.

[36] W.L. Jorgensen, J. Chandrasekhar, J.D. Madura, R.W. Impey, M.L. Klein, Comparison of simple potential functions for simulating liquid water, J. Chem. Phys. 79 (1983) 926–935. https://doi.org/10.1063/1.445869.

[37] A.E. van der Windt, E. Haak, N. Kops, J.A.N. Verhaar, H. Weinans, H. Jahr, Inhibiting calcineurin activity under physiologic tonicity elevates anabolic but suppresses catabolic chondrocyte markers, Arthritis Rheum. 64 (2012) 1929–1939. https://doi.org/10.1002/art.34369.

[38] https://cgenff.paramchem.org/, (n.d.).

[39] K. Vanommeslaeghe, E. Hatcher, C. Acharya, S. Kundu, S. Zhong, J. Shim, E. Darian, O. Guvench, P. Lopes, I. Vorobyov, A.D. Mackerell Jr., CHARMM general force field: A force field for drug-like molecules compatible with the CHARMM all-atom additive biological force fields, J. Comput. Chem. 31 (2010) 671–690. https://doi.org/10.1002/jcc.21367.

[40] K. Vanommeslaeghe, A.D. MacKerell, Automation of the CHARMM general force field (CGenFF) I: Bond perception and atom typing, J. Chem. Inf. Model. 52 (2012) 3144–

3154. https://doi.org/10.1021/ci300363c.
[41] K. Vanommeslaeghe, E.P. Raman, A.D. MacKerell, Automation of the CHARMM General Force Field (CGenFF) II: Assignment of Bonded Parameters and Partial Atomic Charges, J. Chem. Inf. Model. 52 (2012) 3155–3168. https://doi.org/10.1021/ci3003649.
[42] W. Yu, X. He, K. Vanommeslaeghe, A.D. MacKerell, Extension of the CHARMM general force field to sulfonyl-containing compounds and its utility in biomolecular simulations, J. Comput. Chem. 33 (2012) 2451–2468. https://doi.org/10.1002/jcc.23067.
[43] S.E. Feller, Y. Zhang, R.W. Pastor, B.R. Brooks, Constant pressure molecular dynamics simulation: The Langevin piston method, J. Chem. Phys. 103 (1995) 4613–4621. https://doi.org/10.1063/1.470648.
[44] M.G. Paterlini, D.M. Ferguson, Constant temperature simulations using the Langevin equation with velocity Verlet integration, Chem. Phys. 236 (1998) 243–252. https://doi.org/10.1016/S0301-0104(98)00214-6.
[45] T. Darden, D. York, L. Pedersen, Particle mesh Ewald: An N·log(N) method for Ewald sums in large systems, J. Chem. Phys. 98 (1993) 10089–10092. https://doi.org/10.1063/1.464397.
[46] T.R. Forester, W. Smith, SHAKE, rattle, and roll: Efficient constraint algorithms for linked rigid bodies, J. Comput. Chem. 19 (1998) 102–111. https://doi.org/10.1002/(SICI)1096-987X(19980115)19:1<102::AID-JCC9>3.0.CO;2-T.
[47] D.R. Roe, T.E. Cheatham III, PTRAJ and CPPTRAJ: Software for processing and analysis of molecular dynamics trajectory data, J. Chem. Theory Comput. 9 (2013) 3084–3095. https://doi.org/10.1021/ct400341p.
[48] D.A. Case, I.Y. Ben-Shalom, S.R. Brozell, D.S. Cerutti, T.E. Cheatham III, V.W.D. Cruzeiro, T.A. Darden, R.E. Duke, D. Ghoreishi, M.K. Gilson, H. Gohlke, A.W. Goetz, D. Greene, R. Harris, N. Homeyer, S. Izadi, A. Kovalenko, T. Kurtzman, T.S. Lee, S. LeGrand, P. Li, C. Lin, J. Liu, T. Luchko, R. Luo, D.J. Mermelstein, K.M. Merz, Y. Miao, G. Monard, C. Nguyen, H. Nguyen, I. Omelyan, A. Onufriev, F. Pan, R. Qi, D.R. Roe, A. Roitberg, C. Sagui, S. Schott-Verdugo, J. Shen, C.L. Simmerling, J. Smith, R. Salomon-Ferrer, J. Swails, R.C. Walker, J. Wang, H. Wei, R.M. Wolf, X. Wu, L. Xiao, D.M. York, P.A. Kollman, Amber 2018, Univ. California, San Fr. (2018).
[49] W. Humphrey, A. Dalke, K. Schulten, VMD: Visual molecular dynamics, J. Mol. Graph. 14 (1996) 33–38. https://doi.org/10.1016/0263-7855(96)00018-5.
[50] M. Topf, P. Várnai, W.G. Richards, Ab initio QM/MM dynamics simulation of the tetrahedral intermediate of serine proteases: Insights into the active site hydrogen-bonding network, J. Am. Chem. Soc. 124 (2002) 14780–14788. https://doi.org/10.1021/ja026219q.
[51] Y. Zhou, Y. Zhang, Serine protease acylation proceeds with a subtle re-orientation of the histidine ring at the tetrahedral intermediate, Chem. Commun. 47 (2011) 1577–1579. https://doi.org/10.1039/c0cc04112b.
[52] J. Rebek, On the structure of histidine and its role in enzyme active sites, Struct. Chem. 1 (1990) 129–131. https://doi.org/10.1007/BF00675792.